Dear Author,

Here are the proofs of your article.

- You can submit your corrections **online**, via **e-mail** or by **fax**.

- For **online** submission please insert your corrections in the online correction form. Always indicate the line number to which the correction refers.

- You can also insert your corrections in the proof PDF and **email** the annotated PDF.

- For fax submission, please ensure that your corrections are clearly legible. Use a fine black pen and write the correction in the margin, not too close to the edge of the page.

- Remember to note the **journal title**, **article number**, and **your name** when sending your response via e-mail or fax.

- **Check** the metadata sheet to make sure that the header information, especially author names and the corresponding affiliations are correctly shown.

- **Check** the questions that may have arisen during copy editing and insert your answers/ corrections.

- **Check** that the text is complete and that all figures, tables and their legends are included. Also check the accuracy of special characters, equations, and electronic supplementary material if applicable. If necessary refer to the *Edited manuscript*.

- The publication of inaccurate data such as dosages and units can have serious consequences. Please take particular care that all such details are correct.

- Please **do not** make changes that involve only matters of style. We have generally introduced forms that follow the journal's style.
  Substantial changes in content, e.g., new results, corrected values, title and authorship are not allowed without the approval of the responsible editor. In such a case, please contact the Editorial Office and return his/her consent together with the proof.

- If we do not receive your corrections **within 48 hours**, we will send you a reminder.

- Your article will be published **Online First** approximately one week after receipt of your corrected proofs. This is the **official first publication** citable with the DOI. **Further changes are, therefore, not possible.**

- The **printed version** will follow in a forthcoming issue.

Please note

After online publication, subscribers (personal/institutional) to this journal will have access to the complete article via the DOI using the URL: http://dx.doi.org/[DOI].
If you would like to know when your article has been published online, take advantage of our free alert service. For registration and further information go to: http://www.link.springer.com.

Due to the electronic nature of the procedure, the manuscript and the original figures will only be returned to you on special request. When you return your corrections, please inform us if you would like to have these documents returned.

Metadata of the article that will be visualized in OnlineFirst

ArticleTitle	In situ high-temperature XRD and FTIR investigation of hohmannite, a water-rich Fe-sulfate, and its decomposition products	
Article Sub-Title		
Article CopyRight	Akadémiai Kiadó, Budapest, Hungary (This will be the copyright line in the final PDF)	
Journal Name	Journal of Thermal Analysis and Calorimetry	
Corresponding Author	Family Name	**Ventruti**
	Particle	
	Given Name	**G.**
	Suffix	
	Division	Dipartimento di Scienze della Terra e Geoambientali
	Organization	Università di Bari
	Address	via Orabona, 4, 70125, Bari, Italy
	Email	gennaro.ventruti@uniba.it
Author	Family Name	~~**Ventura**~~
	Particle	
	Given Name	**G. Della**
	Suffix	
	Division	Dipartimento Scienze Geologiche
	Organization	Università di Roma Tre
	Address	Largo S. Leonardo Murialdo 1, 00146, Rome, Italy
	Email	
Author	Family Name	**Scordari**
	Particle	
	Given Name	**F.**
	Suffix	
	Division	Dipartimento di Scienze della Terra e Geoambientali
	Organization	Università di Bari
	Address	via Orabona, 4, 70125, Bari, Italy
	Email	
Author	Family Name	**Susta**
	Particle	
	Given Name	**U.**
	Suffix	
	Division	Dipartimento Scienze Geologiche
	Organization	Università di Roma Tre
	Address	Largo S. Leonardo Murialdo 1, 00146, Rome, Italy
	Email	
Author	Family Name	**Gualtieri**

Particle		
Given Name	**A. F.**	
Suffix		
Division	Dipartimento di Scienze Chimiche e Geologiche	
Organization	Università degli Studi di Modena e Reggio Emilia	
Address	L.go S.Eufemia 19, 41121, Modena, Italy	
Email		

Abstract	The thermal dehydration of hohmannite, $Fe_2[O(SO_4)_2] \cdot 8H_2O$, a secondary iron-bearing hydrous sulfate, was investigated by in situ high-temperature X-ray powder diffraction and in situ high-temperature Fourier transform infrared spectroscopy. Combination of the data from both techniques allowed determining the stability fields and reaction paths for this mineral and its high temperature products. Five main dehydration/transformation steps for hohmannite have been identified in the heating range of 25–800 °C. Temperature behavior of the different phases was analyzed, and the heating-induced structural changes are discussed.

In situ high-temperature XRD and FTIR investigation of hohmannite, a water-rich Fe-sulfate, and its decomposition products

**G. Ventruti · G. Della Ventura · F. Scordari ·
U. Susta · A. F. Gualtieri**

Abstract The thermal dehydration of hohmannite, $Fe_2[-O(SO_4)_2]\cdot 8H_2O$, a secondary iron-bearing hydrous sulfate, was investigated by in situ high-temperature X-ray powder diffraction and in situ high-temperature Fourier transform infrared spectroscopy. Combination of the data from both techniques allowed determining the stability fields and reaction paths for this mineral and its high temperature products. Five main dehydration/transformation steps for hohmannite have been identified in the heating range of 25–800 °C. Temperature behavior of the different phases was analyzed, and the heating-induced structural changes are discussed.

Introduction

Metal-sulfate and hydrous metal-sulfate minerals are abundant and ubiquitous on the surface of the Earth in diverse environments including acid mine-drainage wastes [1], acid sulfate soils [2], saline lakes [3], hypogene systems

A1 G. Ventruti (✉) · F. Scordari
A2 Dipartimento di Scienze della Terra e Geoambientali, Università
A3 di Bari, via Orabona, 4, 70125 Bari, Italy
A4 e-mail: gennaro.ventruti@uniba.it

A5 G. D. Ventura · U. Susta
A6 Dipartimento Scienze Geologiche, Università di Roma Tre,
A7 Largo S. Leonardo Murialdo 1, 00146 Rome, Italy

A8 A. F. Gualtieri
A9 Dipartimento di Scienze Chimiche e Geologiche, Università
A10 degli Studi di Modena e Reggio Emilia, L.go S.Eufemia 19,
A11 41121 Modena, Italy

[4], and metallurgical processing plants [5]. They are also known to be present on the surface of Mars [6–9], where they are studied as possible carriers of water [e.g., 10–12].

Iron-bearing sulfate minerals may originate from the weathering of pyrite or pyrrhotite due to bacterial action or to air-oxidation, and are sensitive indicators of environmental conditions such as pH, relative humidity, oxygen activity, and sulfate activity. To obtain information on environmental variables, it is, however, critical to identify and characterize the different species, in terms of chemistry and crystal structure. In addition, knowledge of the properties of sulfates, such as their stability field, transition pathways, and reaction rates, can enhance our understanding of both their technological applications and their use as tracers in geology, and in Mars geology in particular [e.g., 13–15].

Hohmannite, $Fe_2[O(SO_4)_2]\cdot 8H_2O$, (ICSD card no. 98-003-7328) is a hydrated sulfate of ferric iron typically occurring in sedimentary deposits located in areas characterized by arid conditions (e.g., Sierra Gorda, Chile, e.g., [16]). It has been also identified, associated with other metal-bearing sulfates, as an intermediate product in hydrometallurgic plants [17, 18].

To date, limited data on hohmannite and its thermal stability are available. This mineral belongs to a complex series of variably hydrated compounds: hohmannite, metahohmannite, and amarantite [19, 20], which share structural similarities and close stoichiometries, except a variable water content. According to the single-crystal X-ray diffraction studies [21, 22], the structure of hohmannite is based on centrosymmetric $[Fe_4(H_2O)_8O_2(SO_4)_4]$ clusters that polymerize through corner-sharing tetrahedra to form chains of Fe–O–S linkages along the c-axis (Fig. 1). Adjacent chains are linked together by hydrogen bonds involving both water molecules linked to Fe^{3+} ions and free interstitial (H_2O) groups. The hydrogen bond
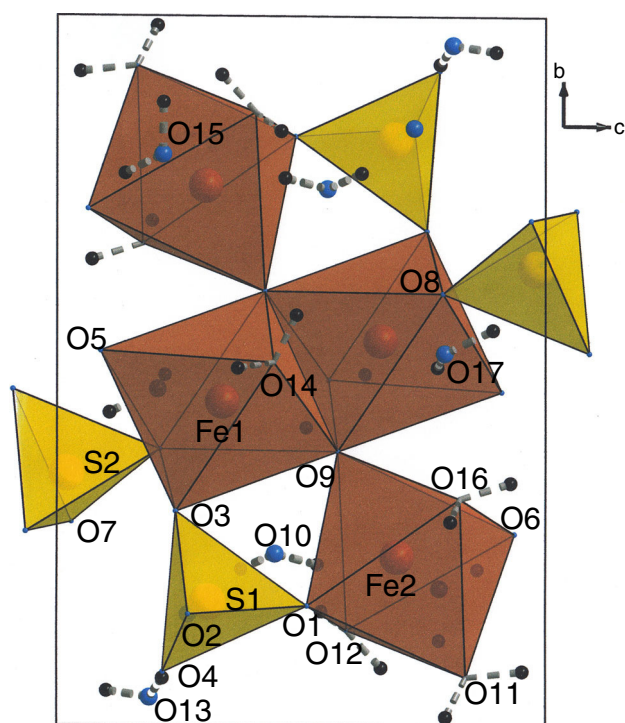
Fig. 1 The crystal structure of hohmannite viewed along the *a* axis, showing the position of the water molecules

65 system has been recently investigated through Fourier
66 transform infrared (FTIR), hydrogen position determina-
67 tion by means of difference-Fourier maps, and verified by
68 detailed bond-valence calculations at all relevant oxygen
69 sites [22]. The thermogravimetric analysis performed by
70 Césbron [23] displays four evident weight losses: a first one
71 of about 15 % starting at ~ 35 °C up to a well-defined
72 plateau from 95 to 140 °C, a second one (~ 12 %) occur-
73 ring in the 140–240 °C range, and a third one (4.5 %)
74 occurring in the 240–560 °C *T* range, while the last step,
75 from around 560 °C up to 700 °C, is associated to a total
76 weight loss of about 32 %. The differential thermal ana-
77 lysis (DTA) [23] shows three distinct endothermic peaks at
78 about 140, 240, and 745 °C, one endothermic shoulder at
79 about 265 °C and one exothermic peak at 525 °C.

80   The aim of this work is to investigate the behavior of
81 hohmannite as a function of increasing temperature by
82 combining in situ XRPD, HT-FTIR, and reference ther-
83 mogravimetric data such as to determine its thermal sta-
84 bility, follow the reaction paths and characterize its high-
85 temperature decomposition products.

Experimental methods

87 The crystals investigated in this study were hand picked
88 under a microscope from the original rock specimen from
89 Sierra Gorda (Chile) from which the sample studied by

90 Scordari [21] had been previously extracted; its chemical
91 composition has been published in [21]. Time-resolved
92 diffraction data were collected at the beamline BM8 (see
93 technical details in [24]) at ESFR (Grenoble, France). The
94 sample was ground in an agate mortar to particle sizes
95 below 400 mesh and packed into a 0.5 mm silica glass
96 capillary open at one end. The capillary was mounted on a
97 standard goniometer head and kept spinning during the
98 collection to increase particle statistics and eliminate pre-
99 ferred orientation effects. Powder data were collected at the
100 fixed wavelength of 0.688808 Å calibrated against the
101 NBS-640b Si standard with $a = 5.43094(4)$ Å at 25 °C.
102 The sample was heated using a heating gun system; the
103 temperature was varied in the range 22–800 °C at
104 5 °C min^{-1} and monitored with a thermocouple located
105 about 0.5 mm below the capillary. During the heating
106 process, powder diffraction patterns were recorded on the
107 3 mm slit-delimited portion of a translating imaging-plate
108 detector system (TIPS), mounted perpendicular to the
109 incoming beam [24]. The heating rate of the experiment
110 was synchronized with the speed of the translating system
111 such as to obtain 72 powder patterns with a temperature
112 step separation of about 11 °C. Powder patterns were
113 extracted in the range 4–45° 2θ with 0.01° 2θ counting step
114 from the stored digitalized file (see [25]) using the original
115 program SCANTIME, developed in house for this purpose.

116   Rietveld refinements were performed using each powder
117 pattern using the GSAS package [26]. The diffraction
118 peaks were modeled using a pseudo-Voigt profile, imple-
119 mented in GSAS as function number two, with one
120 Gaussian (Gw) and two Lorentzian (Lx and Ly) line-
121 broadening coefficients. The background was fitted with a
122 Chebyshev polynomial function using a relatively high
123 number of parameters (19 coefficients) due to the inco-
124 herent contribution of the silica glass capillary. Refinement
125 of the RT pattern was started using the structural model of
126 Scordari [21]. Refinement of metahohmannite obtained
127 from heating hohmannite above 80 °C was carried out
128 using the structural model of Ventruti et al. [20]. Details of
129 the Rietveld refinements at $T = 33$ and 154 °C are reported
130 in Table 1. Refinements of the order–disorder phase FeO-
131 HSO$_4$ [25, 27] obtained from hohmannite at $T > 220$ °C
132 were also performed by DiffaX+ software [28] in order to
133 model stacking faults along the *c*-axis. Starting parameters
134 were taken from Ventruti et al. [25]. Details of the Rietveld
135 refinement at $T = 285$ °C performed with DiffaX+ are
136 also given in Table 1.

137   Single-crystal FTIR HT data were collected using a
138 Bruker Hyperion 3000 microscope at INFN (Frascati) over
139 the 2,000–7,000 cm^{-1} range between 26 and 600 °C. The
140 temperature step was set at 10 °C, for a 10 °C min^{-1}
141 heating rate; the IR spectra were collected immediately
142 when reached the target temperature. For this experiment, a

Table 1 Crystal data and Rietveld refinement parameters of hohmannite at $T = 33$ °C, metahohmannite at $T = 154$ °C, and FeOHSO$_4$ at 285 °C

	$T = 33$ °C	$T = 154$ °C	$T = 285$ °C
Refinement software	GSAS	GSAS	DiffaX+
Formula	Fe$_2$[O(SO$_4$)$_2$] 8H$_2$O	Fe$_2$[O(SO$_4$)$_2$] 4H$_2$O	FeOHSO$_4$
Formula weight	462.92	391.87	168.92
Crystal system	Triclinic	Triclinic	Orthorhombic
Space group	$P\bar{1}$	$P\bar{1}$	$Pnma$
Z	2	2	4
D/g cm^{-3}	2.2446	2.5702	3.3443
Unit cell dimensions			
a/Å	9.1610	7.3379	7.3344
b/Å	10.9279	9.7675	6.4224
c/Å	7.2153	7.1481	7.1666
α/°	90.566	91.669	90
β/°	90.546	98.446	90
γ/°	107.521	86.455	90
Cell volume/Å^3	688.72	504.52	337.53
2θ range/°	4–45	4–45	4–26
Rp/%	7.03	7.30	7.04
Rwp/%	9.46	9.54	7.17

143 cleavage fragment, about 20 μm thick, was placed on a
144 CaF$_2$ sample holder within a LINKAM FTIR600 heating
145 stage. Spectra were collected with a Globar source and a
146 KBr beamsplitter, co-adding 128 scans with a nominal
147 resolution of 4 cm^{-1}.

148 **Experimental results**

149 X-Ray powder diffraction data (XRPD)

150 Examination of the XRPD data shows that hohmannite is
151 stable up to ∼90 °C (Fig. 2). The evolution of the refined
152 cell dimensions reveals a gradual and anisotropic thermal
153 expansion up to 100 °C (Fig. 3). In particular, the a and
154 c parameters increase, with a showing a steeper slope,
155 while the b parameter shows a slightly negative trend. The
156 interaxial angles (Fig. 4) also have different behaviors: α
157 and β decrease, with β showing the largest variation, while
158 γ increases. The cell volume (Fig. 5) shows a linear
159 expansion up to 100 °C. The thermal dependence of lattice
160 parameters and volume of hohmannite over the range
161 22–100 °C were determined by least-squares regression
162 analysis to calculate thermal expansion coefficients [29].
163 The following values were found: $\alpha_a = 9.8(2) \times$
164 10^{-5} K^{-1}, $\alpha_b = -2.4(4) \times 10^{-6}$ K^{-1} and $\alpha_c = 1.9(2) \times$

165 10^{-5} K^{-1}, $\alpha_V = 8.0(7) \times 10^{-5}$ K^{-1}. Axial expansion is
166 strongly anisotropic with $\alpha_a : \alpha_b : \alpha_c = 1 : -0.02 : 0.19$.
167 The hohmannite structure collapses in the T range
168 100–120 °C, while metahohmannite (ICSD card no.
169 98-009-8821) starts growing in the 80–100 °C temperature
170 range, and becomes the predominant phase for $T \geq 110$ °C
171 [20]. This first phase transition is in agreement with the
172 thermal analysis data of Césbron [23]: the abrupt weight
173 loss of 15 %, which occurs in this T range, corresponds
174 with the release of four water molecules from hohmannite
175 (theoretical weight loss 16 %). FTIR spectroscopy (see
176 below) is also in agreement with the water release from the
177 system, although providing a slightly higher T for this
178 transition (∼150 °C).
179 The loss of four water molecules causes the shortening
180 of the chain separations along the a and b crystallographic
181 directions (Fig. 3), the rearrangement of the remaining
182 H$_2$O molecules into a new hydrogen bonding system, and a
183 change in the relative orientation of [Fe$_4$(H$_2$O)$_8$O$_2$(SO$_4$)$_4$]
184 clusters to adapt to the new framework [20]. The backbone
185 of the structure, i.e., the [Fe$_2$(H$_2$O)$_4$O(SO$_4$)$_2$] chain, is,
186 however, topologically the same in both hohmannite and
187 metahohmannite, and this is reflected in the very similar
188 thermal behavior of their cell with T, see the volume as an
189 example (Fig. 5). The thermal expansion coefficients of
190 metahohmannite were determined to be $\alpha_a = 3.8(2) \times$
191 10^{-5} K^{-1}, $\alpha_b = 5.2(4) \times 10^{-6}$ K^{-1}, and $\alpha_c = 3.8(4) \times$
192 10^{-5} K^{-1}, $\alpha_V = 8.5(3) \times 10^{-5}$ K^{-1}. The axial expansion
193 is again strongly anisotropic with $\alpha_a : \alpha_b : \alpha_c = 1 : 0.14 : 1.0$.
194 At about 190 °C, the overall intensity of the metahoh-
195 mannite diffraction reflections starts decreasing with the
196 simultaneous increase of the background, indicating early
197 amorphisation of the sample, while the peaks of the layered
198 phase FeOHSO$_4$, (ICSD card no. 98-002-4079) start
199 showing up. The decomposition of metahohmannite
200 involves the loss of three water molecules directly coor-
201 dinated by the Fe^{3+} ions determining the breakdown of the
202 [Fe$_2$(H$_2$O)$_4$O(SO$_4$)$_2$] chain and the consequent formation of
203 an intermediate amorphous phase from which the FeO-
204 HSO$_4$ compound originates, according to a typical nucle-
205 ation and growth reaction process [25]; notably, the same
206 process was observed in the case of sideronatrite [30] a
207 sodium-iron hydrous sulfate with composition Na$_2$-
208 Fe(SO$_4$)$_2$(OH)·3H$_2$O. This water loss step is again in
209 accordance with the TG data of Césbron [23], which show
210 a weight loss of ∼12 %, in the 140–240 °C range.
211 At about 220 °C, the powder consists of only FeOHSO$_4$;
212 the XRPD data show that this compound is the main phase
213 up to at least 300 °C, while for higher T the diffraction
214 peaks of α-FeSO$_4$ (ICSD card no. 98-002-3907) appear in
215 the assemblage. Ventruti et al. [25] refined the structure of
216 the FeOHSO$_4$ compound and described its order–disorder
217 character as revealed by accurate analysis of the X-ray

Fig. 2 The 3-dimensional plot (2θ-intensity-temperature) extracted by integration of the recorded IP data in the temperature range 33–88 °C
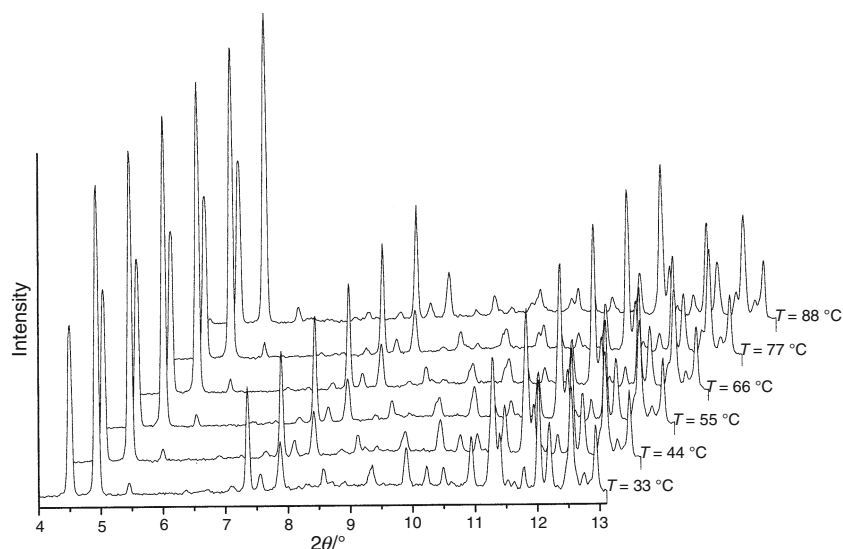
218 pattern. Following their method, successful full-profile
219 refinements of FeOHSO$_4$ at various temperatures were
220 performed here by means of two different methodological
221 approaches: (1) a Le Bail refinement using the Johansson
222 model [31], excluding the Bragg peaks due to stacking
223 disorder; (2) a Rietveld refinement using the DiffaX+
224 software to model the planar disorder for a finite ensemble
225 of equivalent layers stacking along the c-axis direction
226 [25]. Only one layer was sufficient to describe the OD
227 structure; the layer was built up from the Johansson model
228 after the interchange of the b and c axes. All ordered and
229 disordered stacking sequences of equivalent layers were
230 obtained by ranging the α_{11} probability of stacking of
231 equivalent layers by the ($\pm 1/2$, 0, 1) vector and the α_{12}
232 (= $1 - \alpha_{11}$) probability of stacking. The best fit to the
233 observed powder pattern was obtained with $\alpha_{11} = 0.61$.
234 Rietveld refinements were performed for patterns collected
235 in the 230–350 °C range (Fig. 6), where the FeOHSO$_4$
236 compound is the unique or the predominant phase in the
237 powder. Lattice parameters trends determined by both
238 GSAS and DiffaX+ are in agreement. A linear increase of
239 b and c and a decrease of the a cell dimension are
240 observed; the evolution of the cell volume is displayed in
241 Fig. 7. The thermal expansion coefficients for FeOHSO$_4$,
242 calculated between 230 and 350 °C, are $\alpha_a = -8.5(6) \times$
243 10^{-6} K^{-1}, $\alpha_b = 2.9(3) \times 10^{-6} \text{ K}^{-1}$ and $\alpha_c = 1.43(7) \times$
244 10^{-5} K^{-1}, $\alpha_V = 8.6(6) \times 10^{-6} \text{ K}^{-1}$: axial expansion is
245 strongly anisotropic along the stacking direction. At about
246 300 °C, the first diffraction peaks of α-FeSO$_4$ appear; its
247 amount increases slightly up to 500 °C, and then decreases
248 suddenly at 550 °C. Reflection peaks of the rhombohedral
249 Fe$_2$(SO$_4$)$_3$ compound, (ICSD card no. 98-002-2368), are
250 evident (Fig. 8a) in the diffraction pattern of the material
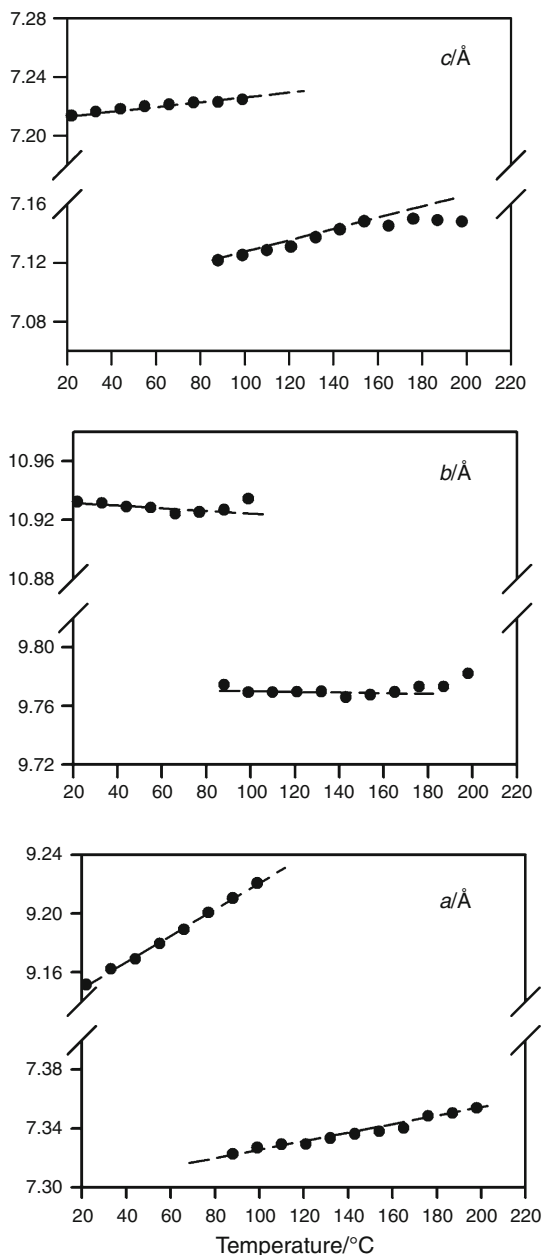251 heated to ~440 °C and persist in the assemblage up to
252 ~750 °C.

253 The X-ray powder pattern at 500 °C shows the first
254 appearance of an unknown phase, as indicated by the dif-
255 fraction peaks at ~11.93, 7.27, 7.21, and 7.11 Å (~7.4°,
256 12.16°, 12.25°, and 12.45° 2θ, respectively, in Fig. 8b).
257 Over the next 50 °C of heating, the intensity of these peaks
258 increases while the FeOHSO$_4$ peaks decrease, and in fact
259 disappear at ~550 °C. This unknown compound is present
260 only in the range 493–668 °C; according to previous
261 studies [32–34], it has a composition Fe$_2$O(SO$_4$)$_2$. Its
262 amount in the assemblage was estimated in a semi-quan-
263 titative way [35] by using the intensity variation of its main
264 reflections at 12.16°, 12.25° (2θ) in the pattern. In partic-
265 ular, being this compound (x phase) chemically and
266 structurally close to FeOHSO$_4$, the density of its unit cell
267 (ρ_x) is assumed to be equal to ρ_{FeOHSO_4}, and the mass
268 absorption coefficient of the mixture (μ^*), normalized to
269 the instrumental-geometric-structural constant (k), is cal-
270 culated using the intensities I_{hkl,FeOHSO_4} whose weight
271 (w$_{\text{FeOHSO}_4}$) is determined from the Rietveld refinements as

$$\mu * / k = \left(\text{w}_{\text{FeOHSO}_4} \bullet I_{hkl,\text{FeOHSO}_4} \right) / \rho_{\text{FeOHSO}_4} \quad \text{(a)}$$

273 At higher temperature, up to 740 °C, hematite α-Fe$_2$O$_3$
274 (ICSD card no. 98-004-0142) is the only predominant
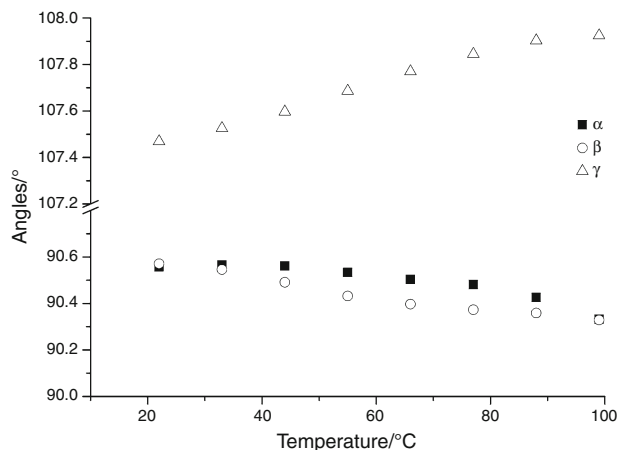275 phase, together with minor Fe$_2$(SO$_4$)$_3$.

In situ HT-FTIR spectroscopy 276

277 ~~In situ~~ evolution of the H$_2$O absorption in the infrared as a
278 function of T can be monitored using bands in different
279 regions of the spectrum: (1) the combination region, where
280 H$_2$O and OH may be distinguished from each other because
281 their contributions occur at different wavenumbers (around
282 5,100 and 4,200 cm^{-1} for H$_2$O and OH, respectively, e.g.,
283 [30, 36]); (2) the stretching region 3,700–3,000 cm^{-1},

Fig. 4 .

Fig. 5 Evolution of the cell volume of hohmannite (20–100 °C range) and metahohmannite (80–200 °C range) calculated by Rietveld refinement of in situ XRPD patterns. Standard deviation is smaller than the used symbols; *broken lines* are a guide for the eye
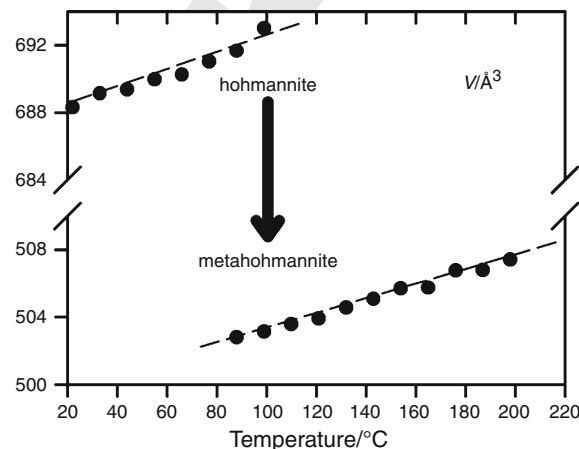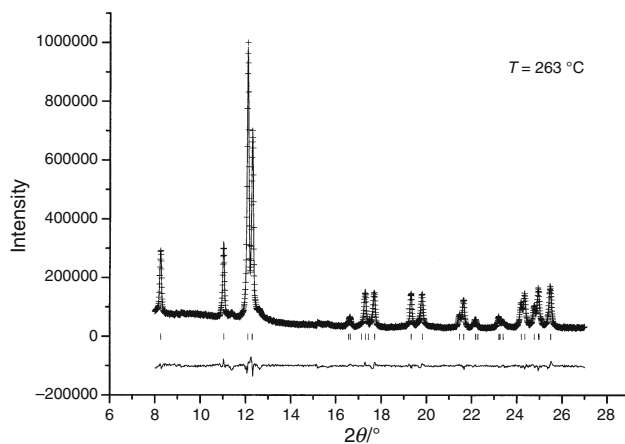
Fig. 3 Evolution of the cell parameters of hohmannite (20–100 °C range) and metahohmannite (80–200 °C range) computed by Rietveld refinement of in situ XRPD patterns. Standard deviations are smaller than the used symbols; *broken lines* are a guide for the eye

284 where the modes of H_2O and OH overlap, and (3) the H_2O
285 bending region (1,600–1,630 cm^{-1}). Unfortunately, for
286 hohmannite the absorption in the principal stretching
287 3,700–3,000 cm^{-1} region is too intense, due to the high
288 water content, thus, the signal at room-T is out of scale,
289 even for crystal thickness of 20–30 μm. For this reason, in
290 the present study, it was chosen to combine the results
291 collected on a single crystal in the H_2O/OH combination
292 and bending regions. The evolution of the H_2O combina-
293 tion mode is displayed in Fig. 9. In this range, the spectra

Fig. 6 Rietveld refinement results for the FeOHSO$_4$ compound. The *crosses* represent the observed data points, and the *smooth line* through them the calculated pattern using DiffaX+
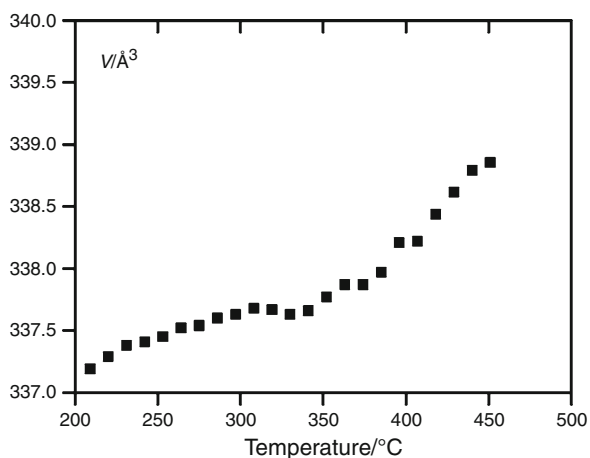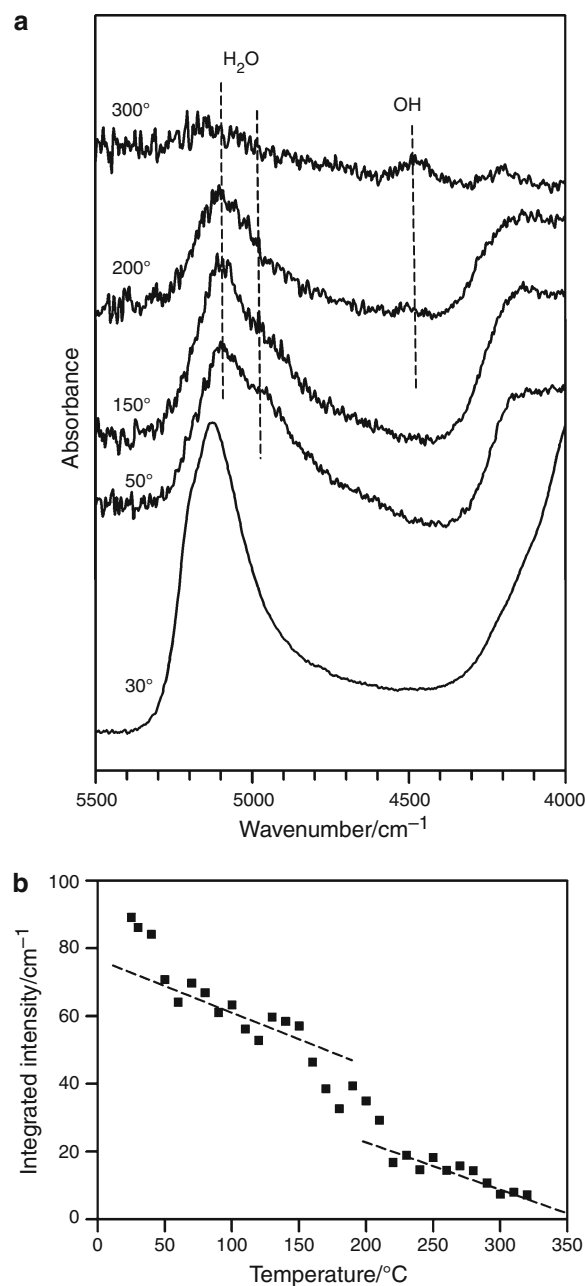
Fig. 7 Evolution of the cell volume of $FeOHSO_4$ (200–450 °C range) determined from the by Rietveld refinement of in situ XRD patterns (data from GSAS). Standard deviations are smaller than the used symbols
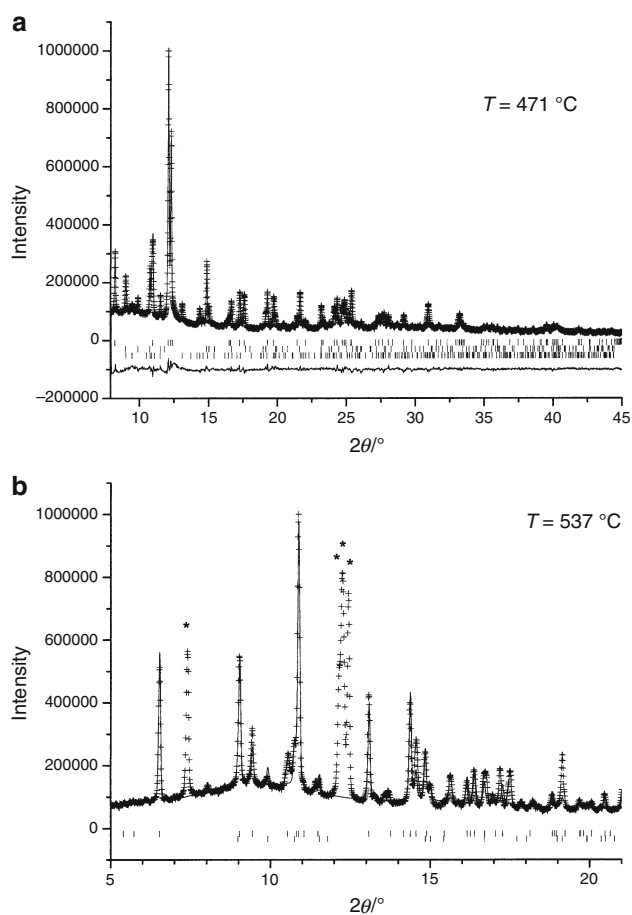

Fig. 8 Observed, calculated and difference powder patterns, from Rietveld refinements of in situ collected data at **a** $T = 471$ °C, and **b** $T = 537$ °C. The *asterisk* symbol indicates peaks of the phase $Fe_2O(SO_4)_2$. For the explanation, see text

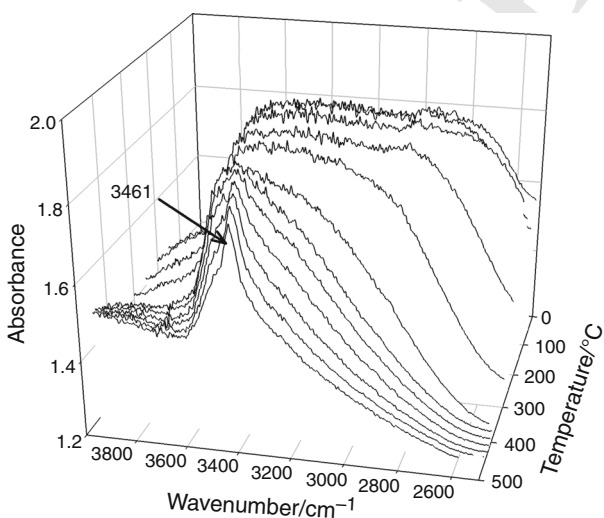Fig. 9 **a** In situ FTIR spectra in the 5,500–4,000 cm^{-1} NIR region; **b** evolution of the integrated intensity of the H_2O combination band at 5,300–4,800 cm^{-1} as a function of increasing T; *broken lines* are a guide for the eye

collected up to 40 °C show a relatively broad band, at 5,128 cm^{-1}, with a shoulder at 5,190 cm^{-1}. The spectrum at 50 °C is significantly different (Fig. 9a), with a much broader band, peaked at 5,046 cm^{-1} and a shoulder at 4,980 cm^{-1}. This pattern remains constant for higher T, and the band gradually reduces its intensity, until complete dehydration. Figure 9b shows a continuous decrease of the band area as a function of T. At ~ 150 °C, the intensity is halved with respect to its original value. For $150 < T < 210$ °C, the dehydration proceeds with a steeper slope; at 210 °C, ~ 20 % of the initial H_2O content is retained in
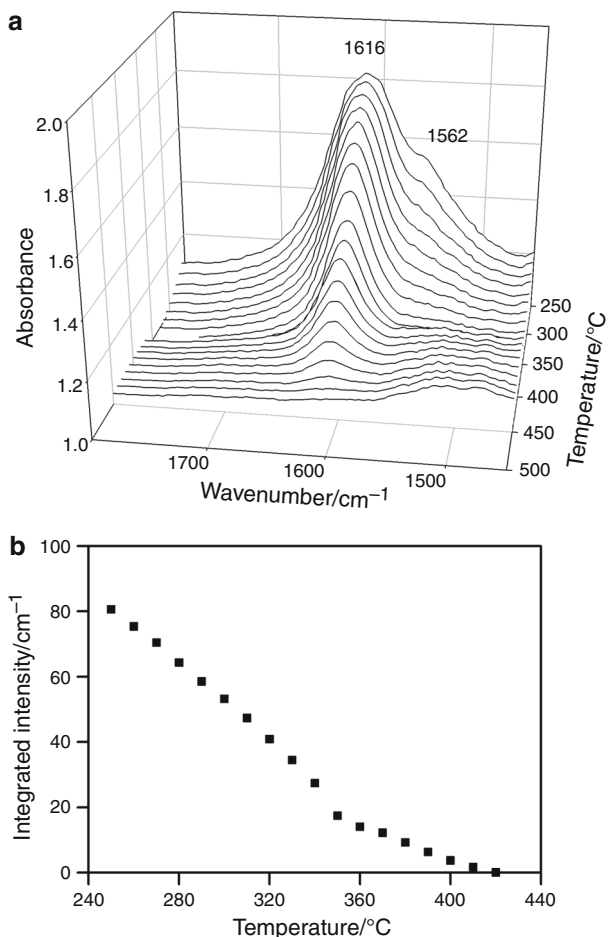
Fig. 10 **a** In situ FTIR spectra in the 1,800–1,400 cm^{-1} region; **b** evolution of the integrated intensity of the H$_2$O bending mode as a function of increasing T


Fig. 11 **a** In situ FTIR spectra in the 4,000–2,500 cm^{-1} region; **b** evolution of the integrated intensity of the H$_2$O stretching mode as a function of increasing T
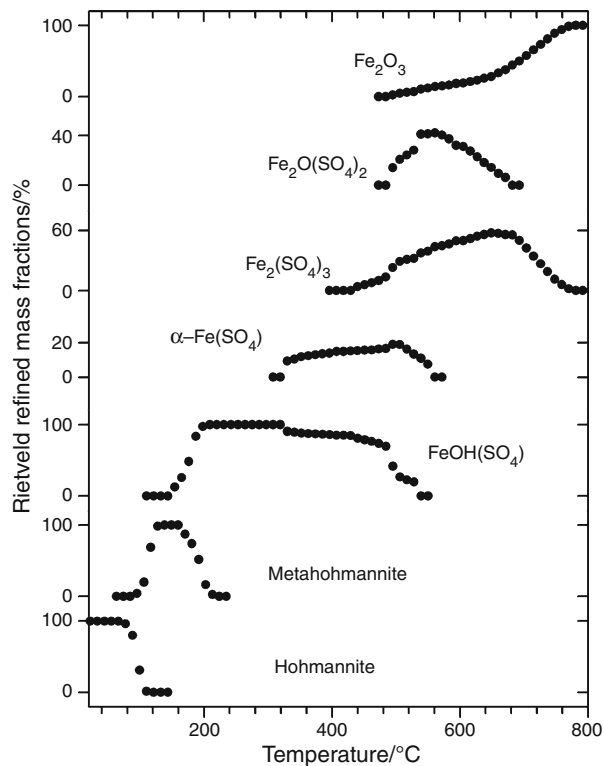
Fig. 12 Rietveld-refined relative amounts of phases due to the thermal treatment of hohmannite over the entire 22–800 °C temperature range. Standard deviation is smaller than the used symbols

the sample; at 350 °C, the combination band is no more visible. For $T < 250$ °C, the H$_2$O bending mode is out of scale; for higher T, it shows two well-evident components at 1,616 and 1,562 cm^{-1}, respectively (Fig. 10a). For $T > 350$ °C, the higher frequency component disappears, and the 1,616 cm^{-1} band keeps decreasing in intensity; at 420 °C it disappears, indicating that at this temperature all H$_2$O has been released. The evolution of the bending peak is displayed in Fig. 10b, where the change in the slope at 350 °C is due to the disappearance of the 1,562 cm^{-1} component. For $T > 420$ °C, a relatively sharp band at 3,461 cm^{-1} is still present in the OH stretching region of the spectrum (Fig. 11). On the basis of the XRD data, this band can be assigned to the OH groups in the FeOHSO$_4$ compound and it disappears above 530 °C.

In summary, analysis of the different H$_2$O/OH bands in the HT-FTIR spectra allows us to conclude that during the heating experiment, under the used conditions, H$_2$O is continuously released from the sample and disappears at 420 °C. At $\sim$210 °C, OH hydroxyl groups appear in the spectra (Fig. 10a), together with the appearance of the FeOHSO$_4$ compound in the system. The OH groups disappear for $T > 530$ °C, in agreement with the diffraction data showing the breakdown of the FeOHSO$_4$ compound at these T conditions.
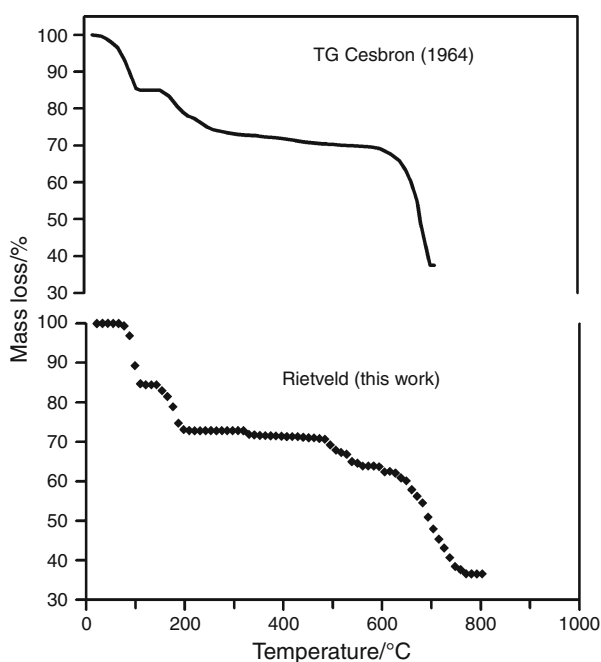
Fig. 13 *Above* TG curve redrawn from the image given in Cesbron (1964); *below* weight loss calculated from the Rietveld-refined phase fractions

Discussion and conclusions

In situ synchrotron X-ray diffraction data combined with IR spectroscopy analysis and with the aid of available TG and DTA data [23] provide insight into the dehydration mechanisms produced during heating of hohmannite, and allows following step-by-step the temperature-induced solid-state transformations as well as the structural changes occurring in this system as a function of increasing temperature.

Rietveld refinement of in situ powder diffraction patterns permitted to identify and quantify (weight fractions) the various phases occurring in the decomposition of hohmannite as a function of temperature. The data are presented in Fig. 12, which displays the complex sequence of structural/chemical transformations occurring in the studied system from RT up to 800 °C.

Examination of Fig. 12 shows that the complete thermal decomposition of hohmannite occurs in five steps. These steps are schematically summarized as follows:

1. first step at 80–120 °C: hohmannite–metahohmannite transition transformation, according to
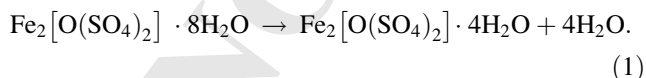
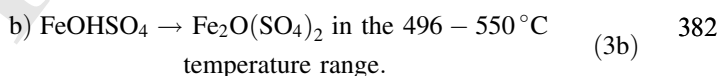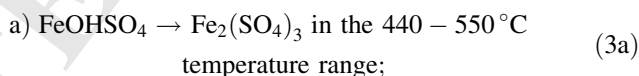$$Fe_2\big[O(SO_4)_2\big] \cdot 8H_2O \rightarrow Fe_2\big[O(SO_4)_2\big] \cdot 4H_2O + 4H_2O. \quad (1)$$

This step involves the release of ~ 15 wt% water, as it is shown by both TG and FTIR data;

2. Second step at 150–220 °C: decomposition of metahohmannite followed by nucleation and growth of FeOHSO$_4$ according to

$$Fe_2\big[(SO_4)_2O\big] \cdot 4H_2O \rightarrow 2FeOHSO_4 + 3H_2O. \quad (2)$$

This step involves the release of ~ 12 wt% water, in accordance with the TG data of Césbron [23]. FTIR spectroscopy shows the appearance of the OH-combination band, and thus of the hydroxyl-bearing Fe-sulfate at 220 °C. The FTIR data in the water bending region $(1,600–1,650 \text{ cm}^{-1})$ show that weak amounts of H_2O, connected with both metahohmannite and the amorphous phase, probably persist up to 420 °C.

3. Third step, occurring in the 330–550 °C T interval: decomposition of FeOHSO$_4$ into several Fe–S–O compounds, according to different possible reactions. FTIR spectra show the presence of OH groups, and thus of Fe-OHSO$_4$ in the solid products, up to 550 °C. The reaction pathway of the thermal decomposition of FeOHSO$_4$ has been studied by several authors (e.g., [32–34, 37, 38]), although subjected to some controversy. Most of these authors observed that the thermal decomposition of FeO-HSO$_4$ is characterized by the formation, at $T > 490$ °C, of an intermediate oxo-sulfate, $Fe_2O(SO_4)_2$, which is decomposed to Fe_2O_3 above 540 °C. Based on our data, we think that much of the controversy is mainly due to a misinterpretation of reflection peaks of FeOHSO$_4$ and $Fe_2O(SO_4)_2$. Our results (Fig. 12) clearly indicate that the decomposition of FeOHSO$_4$ occurs in two main steps:

$$\text{a) } FeOHSO_4 \rightarrow Fe_2(SO_4)_3 \text{ in the } 440 - 550 \,^\circ C \text{ temperature range;} \quad (3a)$$

$$\text{b) } FeOHSO_4 \rightarrow Fe_2O(SO_4)_2 \text{ in the } 496 - 550 \,^\circ C \text{ temperature range.} \quad (3b)$$

~~The α-FeSO$_4$ phase reaches its maximum~~ at $T = 500$ °C, [AQ3] and then quickly decomposes to rhombohedral $Fe_2(SO_4)_3$ up to 550 °C (Fig. 12). This rapid transformation is consistent with the TG data of Césbron [23], which show a sharp and intense DTA exothermic peak at 525 °C. Moreover, our results agree with the data from a combined TG/DSC mass spectroscopy study [39] on the decomposition of FeOHSO$_4$ according to which the mass loss starts at about 400 °C, and two endothermic peaks at 563 and 750 °C are associated with the loss of water and sulfur dioxide, respectively. In particular, it can be noticed from the mass-spectrometry analysis that the water loss increases for $T > 500$ °C and reaches a maximum at 568 °C followed by a sudden drop at $T < 600$ °C, in perfect agreement with the two reactions described above.

4. In the 550–670 °C T range, the $Fe_2O(SO_4)_2$ compound decomposes, according to the reaction:

$$3Fe_2O(SO_4)_2 \rightarrow 2Fe_2(SO_4)_3 + Fe_2O_3 \quad (4)$$
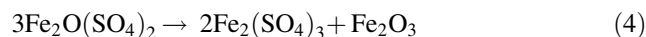
the TG data of Césbron [23] show a total weight loss of about 32 % in this T range which corresponds to the

disruption of SO_4 groups with the subsequent release of SO_2 from the system. Finally,

5. For $T > 670$ °C, there is the disappearance of $Fe_2(SO_4)_3$ to give hematite, according to

$$Fe_2(SO_4)_3 \rightarrow Fe_2O_3 + 3SO_2 + 1.5O_2. \quad (5)$$
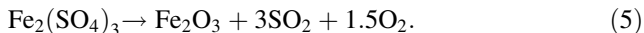
For $T > 750$ °C, only Fe_2O_3 is present in the powder.

The Rietveld-refined weight fractions (Fig. 12) were finally used to simulate the weight loss curve which is displayed in Fig. 13. This curve is in excellent agreement with the experimental thermogravimetric curve reported by Césbron [23], thus supporting both the models used to quantify by XRPD the relative phase fractions in the sample and the described transformation reactions.

References

1. Bai H, Kang Y, Quan H, Han Y, Sun J, Feng Y. Treatment of acid mine drainage by sulfate reducing bacteria with iron in bench scale runs. Bioresour Technol. 2013;128:818–22.
2. Fitzpatrick RW, Fritsch E, Self PG. Interpretation of soil features produced by ancient and modern process in degraded landscapes; V. Development of saline sulfidic features in non-tidal seepage areas. Geoderma. 1996;69:1–29.
3. Glombitza C, Stockhecke M, Schubert CJ, Vetterand A, Kallmeyer J. Sulfate reduction controlled by organic matter availability in deep sediment cores from the saline, alkaline Lake Van (Eastern Anatolia, Turkey). Front Microbiol. 2013. doi: 10.3389/fmicb.2013.00209.
4. Wayne K. Hypogene Karst and sulfate diagenesis of the Delaware Basin: Southeastern New Mexico and Far West Texas, Ph.D Thesis, New Mexico Institute of Mining and Technology, Socorro, New Mexico. 2008.
5. Lawrence RW, Marchant PB, Bratty M, Kratochvil D. Applications for biogenic sulphide reagent for copper recovery in copper and gold hydrometallurgical operations. In: Proceedings of Cu2007, the 6th Copper/Cobre conference, Toronto, August 25–30. 2007.
6. Klingelhöfer G, Morris RV, Bernhardt B, Schröde C. Jarosite and hematite at Meridiani Planum from Opportunity's Mössbauer spectrometer. Science. 2004;306:1740–5.
7. Johnson JR, Bell JF, Cloutis E, Staid M, Farrand WH, McCoy T, Rice M, Wang A, Yen A. Mineralogic constraints on sulfur-rich soils from Pancam spectra at Gusev crater, Mars. Geophys Res Lett. 2007;34:L13202.
8. Vicenzi EP, Fries M, Fahey A, Rost D, Greenwood JP, Steele A. Detailed elemental, mineralogical, and isotopic examination of jarosite in Martian Meteorite MIL 03346. 38th Lunar and planetary science conference, (Lunar and Planetary Science XXXVIII), held 12–16 March 2007 in League City, Texas. LPI Contribution No. 1338, p. 2335.
9. Lane MD, Bishop JL, Dyar MD, King PL, Parente M, Hyde BC. Mineralogy of the Paso Robles soils on Mars. Am Mineral. 2008;93:728–39.
10. Gendrin A, Mangold N, Bibring JP, Langevin Y, Gondet B, Poulet F, Bonello G, Quantin C, Mustard J, Arvidson R, LeMouélic S. Sulfates in Martian layered terrains: the OMEGA/Mars express view. Science. 2005;307:1587–91.
11. Bibring JP, Langevin Y, Mustard JF, Poulet F, Arvidson R, Gendrin A, Gondet B, Mangold N, Pinet P, Forget F, The OMEGA Team. Global mineralogical and aqueous mars history derived from OMEGA/Mars express data. Science. 2006;312:400–4.
12. Wendt L, Gross C, Kneiss T, Sowe M, Combe JPh, LeDeit L, McGuire PC, Neukum G. Mineralogy and stratigraphy of sulfates and ferric oxides in Ophir Chasma, Mars. 42nd lunar and planetary science conference, 1775. 2011.
13. Cloutis EA, Hawthorne FC, Mertzman SA, Krenn K, Craig MA, Marcino D, Methot M, Strong J, Mustard JF, Blaney DL, Bell JF III, Vilas F. Detection and discrimination of sulfate minerals using reflectance spectroscopy. Icarus. 2006;184:121–57.
14. Lu Y, Wang A. Synthesis and spectral characterization of OH-bearing ferric sulfates. XXXXIII Lunar Planet. Sc. Conf., Abstract 2514, Huston. 2012.
15. Spratt H, Rintoul L, Avdeev M, Martens W. The thermal decomposition of hydronium jarosite and ammoniojarosite. J Therm Anal Calorim. 2014;115:101–9.
16. Palache C, Berman H, Frondel C. The system of mineralogy of James Dwight Dana and Edward Salisbury Dana, Yale University 1837–1892, Vol 2, 7th edition. Wiley: New York; 1951.
17. Ngenda RB, Segers L, Kongolo PK. Base metals recovery from zinc hydrometallurgical plant residues by digestion method. Hydrometallurgy Conference 2009. The Southern African Institute of Mining and Metallurgy. Symposium Series 54. 2009. pp. 17–29.
18. Ruhl AS, Kranzmann A. Corrosion behavior of various steels in a continuous flow of carbon dioxide containing impurities. Int J Greenh Gas Control. 2012;9:85–90.
19. Strunz H, Nickel EH. Strunz mineralogical tables. chemical structural mineral classification system 9th edition, 870 S., 226 Abb., Best.-Nr. 13-3509. 2001.
20. Scordari F, Ventruti G, Gualtieri AF. The structure of metahohmannite, Fe + 32[O(SO4)2]·4H2O, by in situ synchrotron powder diffraction. Am Mineral. 2004;89:265–70.
21. Scordari F. The crystal structure of hohmannite, Fe2(H2O)4[(SO4)2O]·4H2O and its relationship to amarantite, Fe2(H2O)4[(SO4)2O]·3H2O. Mineral Mag. 1978;42:144–6.
22. G. Ventruti G, Della Ventura G, Orlando R, Scordari F. Crystal-structure and vibrational spectroscopy of hohmannite, Fe2[(SO4)2O]·8H2O. 2014 (in press).
23. Césbron F. Contribution à la Minéralogie des sulfates de fer-hydratés. Bull Soc Fr Min Cryst. 1964;87:125–43.
24. Meneghini C, Artioli G, Balerna A, Gualtieri AF, Norby P, Mobilio S. Multipurpose imaging-plate camera for in situ powder XRD at the GILDA beamline. J Synchrotron Radiat. 2001;8:1162–6.
25. Ventruti G, Scordari F, Schingaro E, Gualtieri AF, Meneghini C. The order-disorder character of FeOHSO4 obtained from the thermal decomposition of metahohmannite, Fe2+3[O(SO4)2]·4H2O. Am Mineral. 2005;90:679–86.
26. Larson AC, Von Dreele RB. General structure analysis system (GSAS). Los Alamos National Laboratory Report LAUR 86–748. 2000.
27. Gomez MA, Ventruti G, Celikin M, Assaaoudi H, Putz H, Becze L, Leea KE, Demopoulos GP. The nature of synthetic basic ferric arsenate sulfate [Fe(AsO4)1−x(SO4)x(OH)x] and basic ferric sulfate (FeOHSO4): their crystallographic, molecular and electronic structure with applications in the environment and energy. RSC Adv. 2013;37:16840–9.
28. Leoni M, Gualtieri AF, Roveri N. Simultaneous refinement of structure and microstructure of layered materials. J Appl Cryst. 2004;37:166–73.
29. Fei Y. Thermal expansion. In: Ahrens TJ, editor. Mineral physics and crystallography: a handbook of physical constants, vol. 2. Washington: American Geophysical Union; 1995. p. 29–44.

30. Della Ventura G, Ventruti G, Bellatreccia F, Scordari F, Cestelli Guidi M. FTIR transmission spectroscopy of sideronatrite, a sodium-iron hydrous sulfate. Mineral Mag. 2013;77:499–507.

31. Johansson G. On the crystal structure of $FeOHSO_4$ and $InOHSO_4$. Acta Chem Scand. 1962;16:1234–44.

32. Pelovski Y, Petkova V, Nikolov S. Study of the mechanism of the thermochemical decomposition of ferrous sulphate monohydrate. Thermochim Acta. 1996;274:273–80.

33. Petkova V, Pelovski Y. Investigation on the thermal properties of $Fe_2O(SO_4)_2$, part I. J Therm Anal Calorim. 2001;64:1025–35.

34. Petkova V, Pelovski Y. Investigation on the thermal properties of $Fe_2O(SO_4)_2$, part II. J Therm Anal Calorim. 2001;64:1037–44.

35. Klug HP, Alexander LE. X-ray diffraction procedures for poly-crystalline and amorphous materials. New York: Wiley; 1974.

36. Ventruti G, Scordari F, Della Ventura G, Bellatreccia F, Gualtieri AF, Lausi A. The thermal stability of sideronatrite and its decomposition products in the system Na_2O–Fe_2O_3–SO_2–H_2O. Phys Chem Miner. 2013;40:659–70.

37. Swamy MSR, Prasad TP. Thermal analysis of iron(II) sulphate heptahydrate in air. V thermal decomposition of hydroxy and oxysulphates. J Therm Anal Calorim. 1981;20:107–14.

38. Mahapatra S, Prasad TP, Rao KK, Nayak R. Thermal decomposition of hydrolysis products of $Fe(OH)SO_4$. Thermochim Acta. 1990;161:279–85.

39. Schindler A, Blumm, J. Simultaneous thermal analysis of iron hydroxy sulfate. Application note. 2009. http://www.azonano.com/article.aspx?ArticleId=2437.

Springer

the language of science

Author Query Form

Please ensure you fill out your response to the queries raised below and return this form along with your corrections

Dear Author

During the process of typesetting your article, the following queries have arisen. Please check your typeset proof carefully against the queries listed below and mark the necessary changes either directly on the proof/online grid or in the 'Author's response' area provided below

Query	Details Required	Author's Response
AQ1	Please check and confirm the edit made to the article title and amend if necessary.	
AQ2	Please check artwork present in article caption is missing. Kindly check and provide caption for Fig. 4.	
AQ3	Please check and confirm the edits made to the sentence 'The α-FeSO4 phase reaches its maximum at …' and amend if necessary.	